Considerable Unaccounted Local Sources of NO$_x$ Emissions in China Revealed from Satellite

Hao Kong, Jintai Lin,* Lulu Chen, Yuhang Zhang, Yingying Yan, Mengyao Liu, Ruijing Ni, Zehui Liu, and Hongjian Weng

Read Online

ACCESS | 📊 Metrics & More | 📰 Article Recommendations | 🆂🅸 Supporting Information

ABSTRACT: High-resolution (e.g., 5 km) emission data of nitrogen oxides (NO$_x$ = NO + NO$_2$) provide localized knowledge of pollution sources for targeted regulations, yet such data are lacking or inaccurate over most regions at present. Here we improve our PHLET-based inversion method to derive NO$_x$ emissions in China at a 5-km resolution in summer 2019, based on the TROPOMI-POMINO satellite product of nitrogen dioxide (NO$_2$) columns. With low computational costs, our inversion explicitly accounts for the effects of horizontal transport and nonlinear chemistry. We find numerous small-to-medium sources related to minor roads and small human settlements at relatively low affluence levels, in addition to clear emission signals along major transportation lines, consistent with road line density and Tencent location data. Many small-to-medium sources and transportation emissions are unclear or missing in the spatial distributions of four widely used emission inventories. Our emissions offer a unique reference for targeted emission control.

PHLET NOx Emission (kg NO$_2$ km^{-2} h^{-1})

KEYWORDS: *NO$_x$ emission, high resolution, satellite, China, TROPOMI*
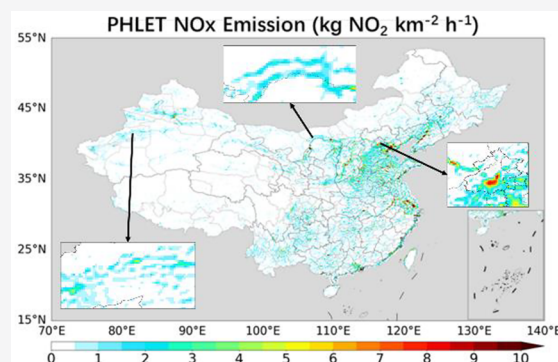
INTRODUCTION

Tropospheric nitrogen oxides (NO$_x$ = NO + NO$_2$) are a major short-lived air pollutant. At present, its emissions are dominated by anthropogenic sources around human settlements of various sizes.[1,2] Since the anthropogenic emissions vary dramatically with intricate human activities from place to place, high-resolution (i.e., 5 km) emission data are critical for understanding the environmental effects of local human activities. Such data provide a fundamental basis for high-resolution (e.g., city- or county-level) air quality modeling and assessment and targeted emission control. However, up-to-date high-resolution NO$_x$ emissions data are still lacking over most regions of the world.

Bottom-up inventories are widely used to estimate NO$_x$ emissions, by combining regional (e.g., provincial) activity data, emission factors, and spatial proxies to downscale emissions to individual locations. These inventories are subject to large uncertainties in emission factors and activity data.[3] Although much effort has been made to locate large point sources in China in a latest 1-km resolution inventory for 2013,[4] about 50% of the total NO$_x$ emissions remain relying on proxy-based downscaling. At fine spatial scales, the proxy-based downscaling approach cannot work well, because emissions are related to these proxies in complex ways. Different choices of proxy can lead to large differences in the spatial distribution of NO$_x$ emissions.[5] Studies have shown that common proxies such as population density tend to be decoupled with NO$_x$ emissions at high resolutions, since large emission sources tend to be away from populous city centers.[4,6] Also, up-to-date high-resolution proxies can be difficult or impossible to obtain; for example, gridded population density data in China are developed based on the census in 2010.[5,7]

Over the past two decades, top-down estimates of NO$_x$ emissions based on satellite retrievals of NO$_2$ vertical column densities (VCDs) have become popular. Traditional top-down approaches assuming local mass balance (LMB) without explicit considerations of horizontal transport and nonlinear NO$_x$ chemistry cannot work properly at high resolutions as the effect of horizontal transport becomes significant.[8−13] More sophisticated methods such as Kalman Filter and Adjoint use iterative simulations of 3-dimensional chemical transport models (CTMs) to account for pollution transport and nonlinear chemistry.[14−16] These methods require expensive computational resources, and are thus difficult to apply to large domains (e.g., East Asia) at high-resolutions (e.g., 5 km).
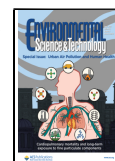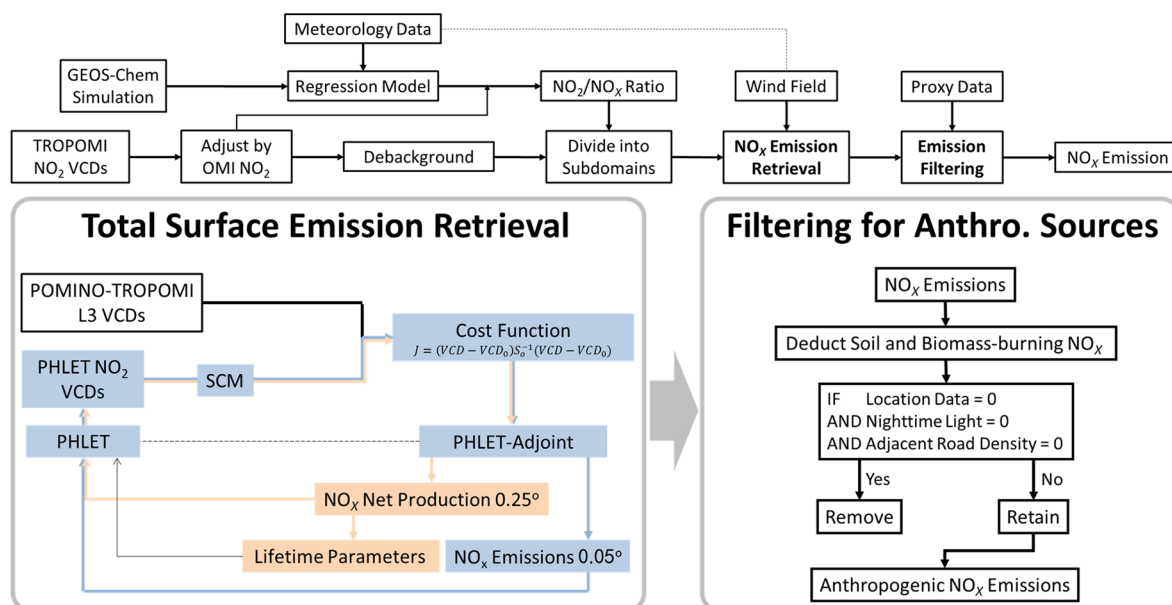
Figure 1. Methodological flowchart of our emission retrieval process. Details of PHLET-based emission inversion in each subdomain and subsequent filtering to obtain "anthropogenic" emissions are shown in the bottom boxes. The orange arrows show the iterative process to retrieve the LNS (Local Net Source, emission minus loss) on a 0.25° × 0.25° grid and determine the lifetime parameters in each subdomain. The blue arrows show the iterative process to retrieve the LNS and NO$_x$ emissions on a 0.05° × 0.05° grid.

A few low-cost inversion methods have been developed recently,[17−21] often for the purpose of estimating individual point sources.[17−19,21] The exponentially modified Gaussian (EMG) model is used to isolate point sources and requires a large number of samples.[17] A regression model based on NO$_2$ column–wind speed relation is developed for a particular topography,[21] and it does not account for the nonlinear dependence of chemical lifetime on NO$_2$ abundance. Another development is the divergence-based model that is dependent on prescribed, fixed NO$_x$ lifetime and CTM-based NO$_2$/NO$_x$ ratios.[18,19] Our previous work[20] develops another fast inversion approach based on a simplified 2-dimensional PHLET (Peking University High-Resolution Lifetime-Emission-Transport) model that takes into account horizontal transport and the nonlinear lifetime-abundance relationship; yet in that study, the method is only applied to a small domain (500 km × 500 km) of the Yangtze River Delta in China.

In this study, we improve our PHLET-based emission inversion approach,[20] and apply it to Asia (70°–140°E, 15°–55°N) at a horizontal resolution of 0.05° × 0.05° in summer (June–August) 2019 based on TROPOMI-POMINO NO$_2$ VCD data. The PHLET model and its adjoint are used for emission inversion. In addition to explicit uncertainty estimates at individual steps of the inversion, we include tests based on NO$_2$ VCDs simulated by GEOS-Chem to further evaluate the overall reliability of our approach. We then analyze the derived emissions for mainland China using five high-resolution spatial proxies of human activity and four widely used bottom-up inventories.

MATERIALS AND METHODS

Figure 1 shows the methodological flowchart. First, NO$_2$ VCDs from TROPOMI are adjusted according to OMI NO$_2$ data to reduce the potential systematic bias. Second, the adjusted TROPOMI NO$_2$ VCDs are used to estimate gridded NO$_2$/NO$_x$ ratios, based on a regression model established by

fitting GEOS-Chem NO$_2$ simulations, air temperature, wind speed, and leaf area index (LAI) data. Third, regional background of NO$_2$ VCDs are estimated and subtracted from the adjusted TROPOMI NO$_2$ data, in order to better reveal the local hot spots of NO$_2$. Fourth, gridded NO$_x$ emissions are derived by applying PHLET and its adjoint model to the adjusted, debackgrounded NO$_2$ VCDs. Finally, to extract the anthropogenic sources, we filter the derived emission data using spatial proxies of human activity.

Tropospheric NO$_2$ VCDs Retrieved from TROPOMI. The TROPOMI sensor is on board the sun-synchronous Copernicus Sentinel-5 Precursor satellite. With a swath of 2600 km, TROPOMI conducts space-borne remote sensing of NO$_2$ globally on a daily basis, with an equator crossing time at 13:30 local time.[22] It has an unprecedentedly high horizontal resolution, with a pixel size of 3.5 × 7 km^2 at nadir (3.5 × 5.5 km^2 since August 2019).[23]

We use the tropospheric NO$_2$ VCD data in summer (June–August) 2019 from the POMINO-TROPOMI product.[24] Compared to the KNMI official product (TM5-MP-DOMINO OFFLINE v1.1.0), POMINO-TROPOMI explicitly accounts for the effects of aerosols and surface reflectance anisotropy on NO$_2$ retrieval, and adopts a priori NO$_2$ vertical profiles at a much higher horizontal resolution (25 km versus 100 km). As a result, POMINO shows a smaller bias of NO$_2$ VCDs than the official product relative to the MAX-DOAS measurements,[24] and has more valid data especially in polluted situations with heavy aerosol and NO$_2$ loadings (e.g., 60% more pixels with NO$_2$ VCD > 5 × 10^{15} molecules cm^{-2}).

Here we conduct a slight update upon POMINO-TROPOMI. The horizontal resolution (25 km) of the a priori vertical profile data of aerosols and NO$_2$ adopted in the POMINO-TROPOMI retrieval process is coarse relative to the size of TROPOMI pixels. This leads to artificial jumps in the profiles among pixels adjacent to the edges of the 25 km-resolution grid cells. To reduce the effect on retrieved NO$_2$, we

interpolate the NO_2 and aerosol profiles to a 5 km-resolution grid (Supporting Information (SI) Figure S1).

The official KNMI TROPOMI NO_2 product is significantly underestimated (25%−50%) globally.[22,24−26] Although PO-MINO-TROPOMI reduces such underestimation, we choose to conduct further correction with the help of POMINO-OMI v2.0.1 NO_2 data.[27−29] According to validation based on MAX-DOAS measurements, POMINO-OMI NO_2 data contain small biases (−3%);[28−30] and OMI NO_2 are often used to help evaluate TROPOMI data.[31] Specifically, we sample the OMI and TROPOMI NO_2 VCD data for summer 2019 within the study domain at a horizontal resolution of 0.25° × 0.25° (given that the pixel size of OMI is 13 × 24 km^2 at nadir), regress the two data sets to obtain the slope (1.08) and intercept (0.29 × 10^{15} molecules cm$^{−2}$) ($R = 0.94$, SI Figure S2a), and then use the slope and intercept to adjust TROPOMI data on a 0.05° × 0.05° grid. To obtain valid data from both sensors, we remove the pixels with cloud radiance fraction exceeding 50%, with AOD larger than 3, or with raw anomaly issues (for OMI data only), following normal practice.[28−30] SI Figure S2b,c presents the POMINO-TROPOMI NO_2 VCDs before and after the adjustment. The mean value of NO_2 VCDs is increased by 31.2% by the adjustment, and thus the underestimate is reduced.

We map the pixel-by-pixel (i.e., Level-2) POMINO-TROPOMI NO_2 data to a 0.05° × 0.05° grid. Following Kong et al. (2019),[20] we use a special oversampling approach to properly assign each irregularly shaped pixel to respective grid cells. We also calculate a satellite conversion matrix (SCM) to facilitate subsequent conversion from PHLET-modeled NO_2 data on the 0.05° × 0.05° grid to each TROPOMI pixel and then back to each PHLET grid cell. The SCM accounts for the difference in shape, size, and geolocation between each satellite pixel and PHLET grid cell. The use of SCM ensures exact matching of satellite and PHLET model data, which is important for high-resolution emission inversion.[20]

Derivation of NO_2 to NO_x Ratio. Inversion of NO_x emissions from NO_2 VCDs requires knowledge on the NO_2/NO_x ratio (r), which has often been assigned a constant value of 0.76 without accounting for its spatially heterogeneous dependence to the NO_x chemistry.[20,21,32] To better link NO_2 VCDs and NO_x emissions, here we establish a regression model to estimate the NO_2/NO_x ratio at each location for subsequent emission inversion. The regression is based on GEOS-FP assimilated 2-m air temperature (T) and lower tropospheric (0−500 m above the ground) wind speed (V) data,[33] reprocessed MODIS v6 LAI data,[34,35] and NO_2 and NO_x concentrations from GEOS-Chem v12.9.3[36] simulations for summer 2019 driven by GEOS-FP meteorological data. GEOS-Chem runs at a horizontal resolution of 0.3125° longitude ×0.25° latitude (see SI Section 1), and all other data are regridded to this resolution.

$$\frac{r}{1+r} = a \cdot \ln\left(\frac{C_{NO_2}}{C_{NO_2}^s}\right) + b \cdot \ln(C_{NO_2}^s) + c \cdot V + d \cdot T + e \cdot LAI + f + \varepsilon$$

(1)

Here, C_{NO_2} refers to tropospheric NO_2 VCDs, $C_{NO_2}^s$ refers to the average C_{NO_2} within a distance of 125 km of each grid cell. The coefficients to be fitted include a, b, c, d, and f. Each of a, b, and f has one value for over land and the other value for over sea. f is the offset, and ε is the residual error. The first term on

the right-hand side highlights local hot-spots above the regional background of NO_2, and the second term represents the regional NO_2 background. The use of LAI represents the effects of biogenic volatile organic compounds on the NO_x chemistry and r.

SI Table S1 summarizes the regression results. SI Figure S3 shows the scatter plot of the NO_2/NO_x ratio explicitly simulated by GEOS-Chem and the ratio predicted based on the regression model. Clearly, the regression model captures the GEOS-Chem simulated NO_2/NO_x ratio ($R = 0.97$, RMSE = 0.03 or ∼5%). The regression model is then applied to the gridded, adjusted POMINO-TROPOMI NO_2 VCDs to derive the respective local NO_2/NO_x ratios at the 0.05° × 0.05° resolution. According to the RMSE above, use of the predicted ratio is assumed to contribute 5% of NO_2 VCDs to the inversion error.

Removal of Regional Background NO_2 VCDs. NO_x emissions from lightning and aircrafts as well as vertical transport of ground-emitted NO_x can lead to NO_2 at high altitudes (i.e., in the free troposphere). Over the anthropogenic source regions, although the NO_2 aloft has a lower concentration than the NO_2 near the ground, it has a longer lifetime, experiences stronger winds, and thus exhibits a smoother horizontal distribution pattern.[20] The NO_2 aloft provides an important regional background. To reduce its influence on our high-resolution emission inversion and better reveal emission hot spots, we remove the NO_2 background before the emission retrieval process.

We identify the regional background contribution to NO_2 VCD at each 0.05° × 0.05° grid cell as follows. First, we calculate the 1% quantile value of its surrounding grid cells within 500 km, with the consideration that NO_2 over clean areas are mainly contributed by the background. We then calculate a 500-km moving average of the 1%-quantile data to reduce noise in the regional background data. This leads to background NO_2 VCDs varying from 0.68 × 10^{15} to 1.38 × 10^{15} molecules cm$^{−2}$ over the study domain, with an average of 0.90 × 10^{15} molecules cm$^{−2}$. The background removal procedure is assumed to contribute 0.30 × 10^{15} molecules cm$^{−2}$ to the inversion error. SI Figure S2d presents the final (i.e., postadjustment, background-removed) NO_2 VCDs to be used in the subsequent emission inversion.

High-Resolution NO_x Emission Inversion. Two main steps to derive NO_x emissions based on the adjusted, debackgrounded NO_2 VCDs are shown at the bottom of Figure 1, including (1) emission inversion by the 2-dimensional model PHLET and its adjoint, and (2) extraction of anthropogenic contributions to the derived emissions.

In the first step, our PHLET-based retrieval is not applied to the whole study domain (70°−140°E, 15°−55°N) at once, which would otherwise lead to a substantial increase in the computational costs and in the uncertainty of fitted parameters describing the nonlinear relationship between NO_2 VCD and lifetime. Rather, we divide the study domain into 405 subdomains (sizing at 5° × 5° each, SI Figure S4) to ensure localization of fitted lifetime parameters and reduce computational costs. The size of each subdomain is the same as in Kong et al. (2019).[20] The adjacent subdomains (5° × 5°) overlap each other by 2.5° on longitude and/or latitude. For each grid cell, its derived emission is determined as the average of emission values derived from individual subdomains encompassing the grid cell, weighted by the square of the reciprocal
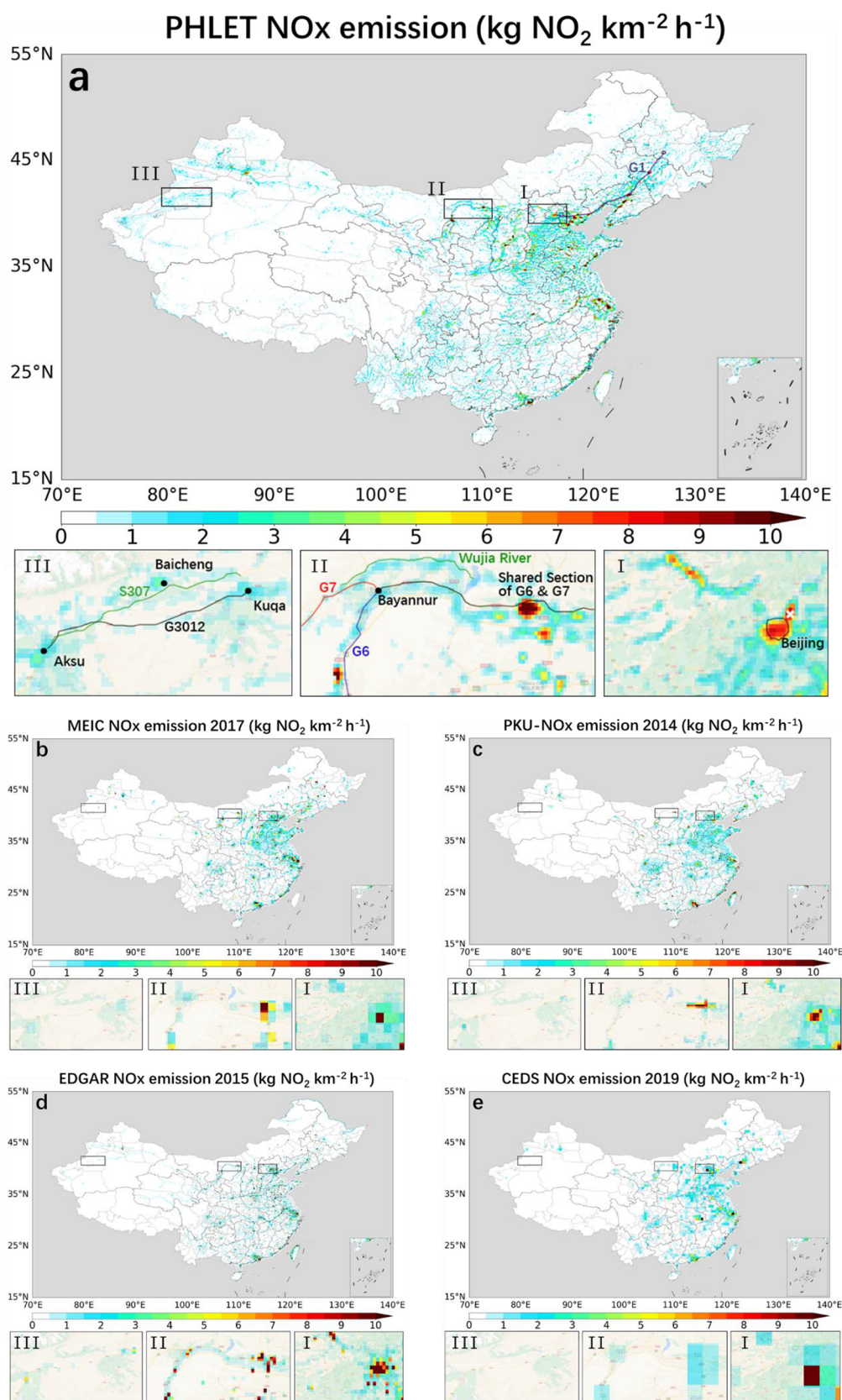
Figure 2. Horizontal distribution of anthropogenic NO_x emissions over China from our PHLET-based emission estimate for summer 2019 at $0.05° \times 0.05°$ (a), MEIC for summer 2017 at $0.25° \times 0.25°$ (b), PKU-NO_x for summer 2014 at $0.1° \times 0.1°$ (c), EDGAR for summer 2015 at $0.1° \times 0.1°$ (d), and CEDS for summer 2019 at $0.5° \times 0.5°$ (e). Three small areas are enlarged to highlight the local signals (I: Beijing; II: Hetao Plain; III: west Xinjiang).

of the distance between the grid cell center and each subdomain center.

Emission Inversion in Each Subdomain. Within each $5° \times 5°$ subdomain, we improve the PHLET-based inversion method[20] to quantify NO_x emissions (Figure 1). The model is based on the following equations that account for emissions, nonlinear chemistry, horizontal flux, and "effective" diffusion of NO_x, as detailed in Kong et al. (2019):[20]

$$\frac{\partial C(x, y)}{\partial t} = r(x, y) \cdot L(x, y) - \nabla \cdot (V(x, y) \cdot C(x, y))$$
$$+ \nabla \cdot (\alpha \cdot K(x, y) \cdot \nabla C(x, y)) = 0 \tag{2}$$

$$L(x, y) = E(x, y) - \frac{C(x, y)}{r(x, y) \cdot \tau(x, y)} \tag{3}$$

$$-a'(r(x, y) \cdot L(x, y) + kC(x, y)) - b' \left(\frac{r(x, y) \cdot L(x, y)}{C(x, y)} + k \right) + c'$$
$$\left(\frac{r(x, y) \cdot L(x, y) + kC(x, y)}{C(x, y)^2} \right)^2 = 1, \text{ where } E(x, y) \approx 0 \tag{4}$$

$$\frac{1}{\tau} = \frac{1}{\tau_c} + k \tag{5}$$

Here, eq 2 presents the governing equation for NO_2; eq 3 defines the local net source (LNS, emission minus loss); eq 4 describes the nonlinear relationship between lifetime and VCD of NO_2; and eq 5 defines the lifetime. C refers to the NO_2 VCD, L the LNS, E the emission, r the NO_2/NO_x ratio, τ the lifetime, τ_c the VCD-dependent chemical lifetime, and k the loss rate constant due to deposition. The values of k, a', b', and c' are to be fitted. V denotes the mean wind vector over the study time period (summer 2019), and K denotes the effective diffusion coefficient tensor to account for horizontal transport by the residual winds deviating from the temporally average wind field. V and K are derived from the GEOS-FP 3-hourly wind field data near the surface (0−500 m above the ground, as a common practice[17,19,20,37−39]) at a horizontal resolution of $0.3125°$ longitude $\times 0.25°$ latitude. As an improvement upon Kong et al. (2019),[20] here we add a scaling factor ($\alpha = 0.5$) to adjust the values of diffusion coefficients, after testing different values from 0.1 to 1.0. A test applying the emission inversion procedure to GEOS-Chem simulated NO_2 VCDs shows that unscaled coefficients would lead to an overestimate in the horizontal transport of NO_2 and thus in the horizontal gradient of derived NO_x emissions.

Based on the PHLET model, its adjoint and the adjusted, debackgrounded POMINO-TROPOMI NO_2 VCDs, we first derive the LNS on a $0.25° \times 0.25°$ grid in order to fit the lifetime parameters (k, a', b', and c' in eq 4). Fitting lifetime parameters based on the LNS data at a resolution of $0.25° \times 0.25°$ rather than $0.05° \times 0.05°$ reduces noise in the fitted parameters. To fit the lifetime parameters, as detailed in Kong et al. (2019),[20] we make use of the relatively clean regions where the emission is small enough to be neglected and thus the LNS is dominated by the loss term ($L(x, y) \approx -\frac{C(x, y)}{r(x, y) \cdot \tau(x, y)}$). These small-emission, clean regions are selected as having low NO_2 VCDs ($<1.5 \times 10^{15}$ molecules cm^{-2}) and low LNS values (at 1% quantile). The lifetime parameters are then derived through nonlinear quantile fitting for the 1%-quantile LNS data as a function of VCDs. The fitting-related uncertainty for derived emissions is estimated by

conducting the fitting procedure at other quantile thresholds (0.1% and 2%, see SI Table S3). We then apply the determined lifetime parameters to rederive LNS and estimate NO_x emissions on a $0.05° \times 0.05°$ grid.

Uncertainty in Emission and Lifetime Estimates. The uncertainty in NO_x emissions derived in each subdomain comes from three major sources; a step-by-step uncertainty estimate follows Kong et al. (2019)[20] with necessary updates detailed in SI Table S3. First, the uncertainty in gridded NO_2 VCDs is associated with the NO_2 retrieval process for each pixel, subsequent long-term averaging for NO_2, and removal of the NO_2 background. Since the pixel-specific NO_2 data are then temporally averaged, the random component of errors is reduced. Combining data from multiple days is a common practice for top-down emission assessments[17,19,20,37−39] to reduce the effect of random errors and missing values in satellite data sets.

Second, the PHLET-related uncertainty is derived from temporal averaging of NO_2 over summer 2019, assumption of stable NO_2 (emission equals loss) at the overpass time of satellite, fitting for the NO_2/NO_x ratio, and assumption of the 2-dimesional process with long-term average horizontal flux and effective diffusion. These two error sources affect the estimate of LNS, with individual sources of errors added in quadrature to establish the diagonal of error covariance matrix of the cost function in PHLET Adjoint.

Third, the uncertainty associated with division of the LNS into emission and loss is derived from fitting of the relationship between NO_2 VCD and lifetime. A uniform relation between NO_2 VCD and NO_x lifetime is assumed and derived in each subdomain of $5° \times 5°$ to retain local features of the nonlinear chemistry. In reality, the VCD-lifetime relationship within a subdomain may not exactly follow a single parametrized formula. The associated error is reflected in part in the uncertainty of fitted parameters and lifetimes. We find that the NO_x lifetimes fitted from (up to) four subdomains covering each grid cell are within 15% for most grid cells, with an average of 10.8%. The respective error is reduced by averaging the results (weighted by the square of the reciprocal of the distance between each grid cell and the subdomain center) from those four subdomains.

For most grid cells, emissions estimated from four subdomains are weighted averages, so are their uncertainties. SI Figure S5a,b shows the spatial distributions of emission uncertainties ($1-\sigma$) in absolute and relative terms, respectively. As expected, the absolute uncertainties tend to be larger (by up to 7.66 kg NO_2 km^{-2} h^{-1}) over high-emission grid cells, and the relative uncertainties tend to be larger over low-emission grid cells. The spatial correlation between the derived emissions (Figure 2a) and their absolute uncertainties (SI Figure S5a) is about 0.55.

SI Figure S5c,d further shows the horizontal distributions of estimated lifetimes and their absolute uncertainties ($1-\sigma$). The lifetimes are about 1.5−3.5 h over most of the high-emission regions of East Asia and South Asia, with uncertainties of 0−1.5 h. The lifetimes are the highest (>5 h) over regions of low anthropogenic emissions such as the oceans and Mongolia, so are their uncertainties (>3 h). Especially over land, the lifetimes are smoother in space than the respective emissions.

We further use GEOS-Chem simulations to test the reliability of our emission inversion approach, following Kong et al. (2019).[20] First, we use the nested GEOS-Chem v12.9.3[36] to simulate the NO_2 VCDs around the overpass time

of TROPOMI in summer 2019 on a 0.3125° longitude ×0.25° latitude grid over Asia. A brief description of model setup is presented in SI Section 1. The simulated NO_2 VCDs are shown in SI Figure S6a. Then the simulated VCDs are regridded to 0.05° × 0.05° and debackgrounded, following the procedures described above for TROPOMI data. Finally, we apply our emission inversion approach to derive the emissions at 0.05° × 0.05°, regrid them to 0.3125° longitude ×0.25° latitude (SI Figure S6b), and compare them to the emissions used in GEOS-Chem (SI Figure S6c) at the same resolution. SI Figure S6d shows that the derived emissions match the GEOS-Chem emissions, with a correlation coefficient of 0.94, a slope of 0.97 and a normalized mean bias of −1.8%.

The above test with GEOS-Chem does not apply the averaging kernels (AKs) of POMINO-TROPOMI. Given that the AKs are embedded in satellite NO_2 VCD data, we conduct another test in which we apply the POMINO-TROPOMI AKs to the GEOS-Chem NO_2 profiles and sample the GEOS-Chem NO_2 VCDs accordingly, before using them as input to retrieve NO_x emissions. [Note that since there are missing values in satellite data, this unavoidably affects the subsequent test.] The resulting retrieved NO_x emissions still agree well with the original emissions used in GEOS-Chem ($R = 0.92$ and NMB = −3.7%, SI Figure S7). There are some underestimates over parts of southern China and overestimates over parts of the North China Plain, similar to the test without applying the AKs (SI Figure S6). This result indicates a minor influence of AKs.

Extraction of Anthropogenic Contributions from Inferred Emissions. Over the study domain, the derived emissions on a 0.05° × 0.05° grid contain the contributions from anthropogenic, biomass burning (open fires) and soil sources. To further identify anthropogenic sources, we subtract from the derived emissions the contributions of biomass burning and soil (SI Figure S8). For this purpose, we adopt the soil NO_x emissions from Weng et al. (2020)[40] and the biomass burning emissions from GFED4;[41] these emissions are interpolated to 0.05° × 0.05° by area weighting, and they together contribute about 11% of the emission total over the study domain.

Then, we examine whether the residual "anthropogenic" NO_x emissions match three main proxies for human activity, including nighttime light (SI Figure S9a), traffic line data (SI Figure S9b,c), and Tencent location (SI Figure S9d). The proxy data are described in SI Section 2 and regridded to 0.05° × 0.05° by area weighting. We remove the emissions on grid cells for which none of the proxies indicate any human activities (Figure 1). For mainland China, the emissions removed amount to about 10%. Note that those emissions removed may not necessarily be of natural origin or artifact of inversion; they are excluded due to lack of ancillary data for further evaluation.

RESULTS AND DISCUSSION

Fine-Scale Characteristics of Derived Anthropogenic Emissions. Figure 2a shows the spatial distribution of derived on-land "anthropogenic" NO_x emissions over China on a 0.05° × 0.05° grid for summer 2019. We focus the analysis on Chinese emissions and mask emissions outside the country and over the oceans, because the Tencent location data used to facilitate data analysis are less reliable outside China. The emissions total 24.75 ± 5.98 Tg NO_2 a^{-1} (scaled based on the amounts of days in a summer and a year) for mainland China and show clear local details.

Regionally, NO_x emissions are the highest over the North China Plain (including Beijing, Tianjin, Hebei, Henan, Shandong, Jiangsu and Anhui provinces), which contributes 30.1% (7.45 ± 1.71 Tg NO_2 a^{-1}) of the total emission in mainland China. In the northeast, emission sources gather around the G1 Expressway connecting the provincial capitals of Liaoning, Jilin and Heilongjiang provinces. The three provinces together contribute 11.4% (2.81 ± 0.69 Tg NO_2 a^{-1}) of the total emission in mainland China. Emissions are also large in the Yangtze River Delta (including Shanghai, Jiangsu, Anhui, and Zhejiang provinces) and Guangdong Province (encompassing the Pearl River Delta), contributing 10.7% (2.64 ± 0.76 Tg NO_2 a^{-1}) and 3.1% (0.77 ± 0.23 Tg NO_2 a^{-1}) of the total in mainland China, respectively. In the western regions, large emission sources are evident around the major cities (e.g., provincial capitals).

More importantly, there are clear fine-scale features at this resolution. The emission hot spots are obvious at the urban areas of each city. There are significant emissions along the traffic lines connecting major cities across the country, most apparently over the west and south, consistent with the road line data set (SI Figure S9b,c). Our emission data also reveal numerous small-to-medium sources spreading across the vast areas of the country, which are hardly seen in bottom-up inventories (see next section). These emissions are often in the suburban and rural areas and near small roads, consistent with the distributions of nighttime light (SI Figure S9a) and Tencent location data (SI Figure S9d).

Comparison with Bottom-up Anthropogenic Emission Inventories. We further compare the derived anthropogenic emissions to four bottom-up anthropogenic inventories, including the Multi-Resolution Emissions Inventory of China (MEIC v1.3, for summer 2017 at 0.25° × 0.25°),[42,43] the Emission Database for Global Atmospheric Research (EDGAR v5.0, for summer 2015 at 0.1° × 0.1°),[44] the Community Emissions Data System (CEDS v2021_04_21, for summer 2019 at 0.5° × 0.5°),[45] and Peking University NO_x (PKU-NO_x v2, for summer 2014 at 0.1° × 0.1°).[46] For each inventory, we use available data in the year closest to 2019. According to CEDS, the emissions decrease by 11.9% from 2014 to 2017 with high spatial correlation ($R = 1.00$) between the two years, and by 3.2% from 2017 to 2019 ($R = 1.00$). According to MEIC, the emissions in 2017 are lower than in 2014 by 14.8% ($R = 0.99$). The interannual variability in the spatial patterns of bottom-up emissions is negligible.

Figure 2 compares the horizontal distributions of different emission data. Our emissions regridded to lower resolutions are shown in SI Figure S10. The MEIC (21.15 Tg NO_2 a^{-1}), EDGAR (26.37 Tg NO_2 a^{-1}), CEDS (22.83 Tg NO_2 a^{-1}) and PKU-NO_x (25.04 Tg NO_2 a^{-1}) emission totals for mainland China are all within 15% of ours (24.75 Tg NO_2 a^{-1}). The large-scale spatial distribution of our emissions is similar to the bottom-up inventories, while there are much more small-to-medium sources in our emissions.

The most important difference between our emission data and bottom-up inventories lies in the fine-scale features. To illustrate this point, Figure 2 shows enlarged emission maps for three small areas including Beijing, the Hetao Plain, and west Xinjiang. In the Beijing area (Figure 2a−d_I), our data show large emissions along the traffic lines connecting Beijing and its surrounding cities, and the emissions of Beijing concentrated within the Fifth Ring Road (denoted by the black circle in Figure 2a_I, with an average of 6.98 ± 2.07 kg NO_2 km^{-2} h^{-1}).

NOx emission amounts in each province
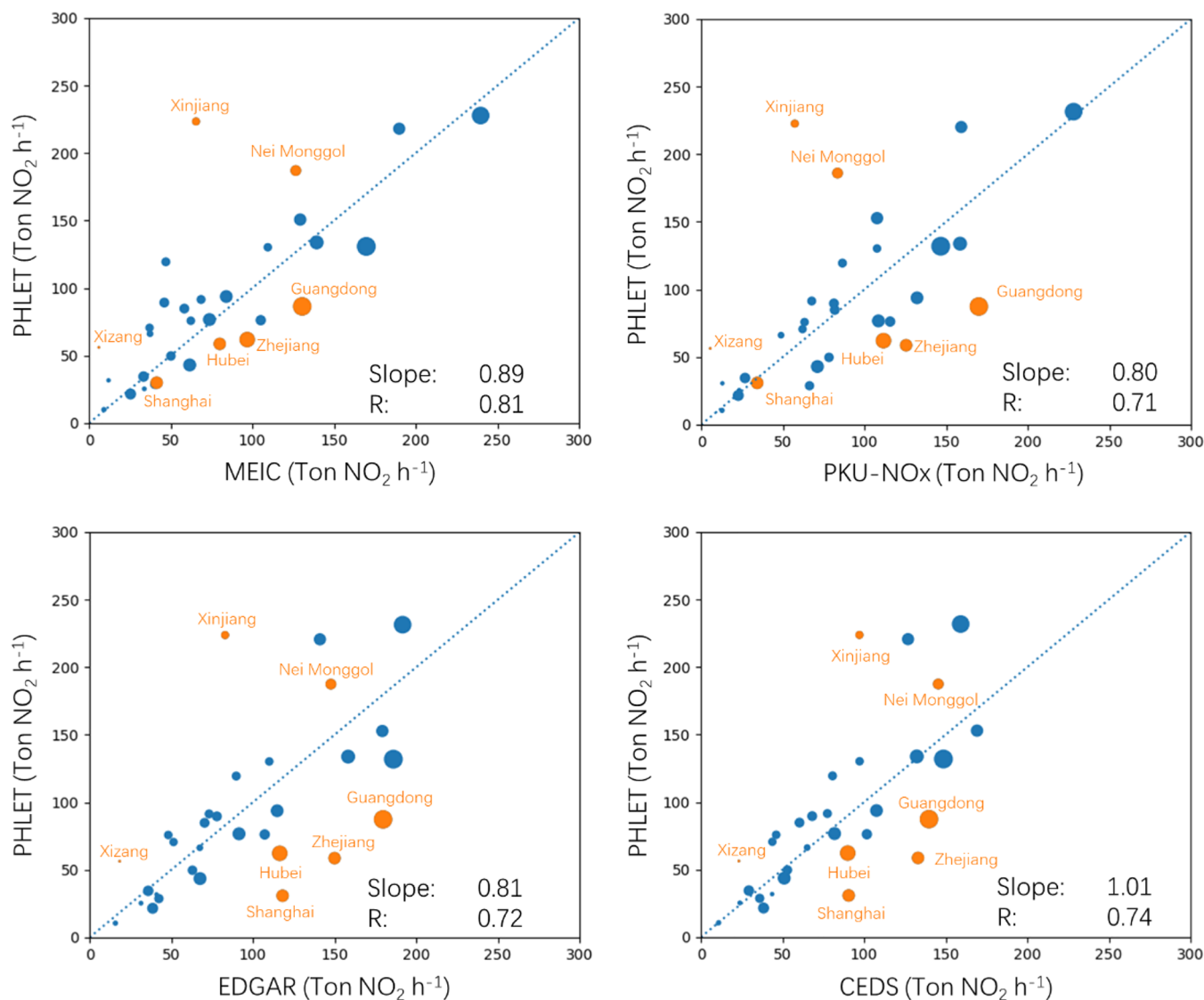
Figure 3. Scatter plots for provincial emissions between our and other data sets for 31 provinces in mainland China. Taiwan, Hong Kong, and Macau are not included. The sizes of the circles indicate the GDP value of each province in 2015. The yellow circles stand for the provinces explicitly mentioned in the main text.

There is a clear emission signal around the highway connecting the urban center and the Beijing Capital International Airport (denoted by the white cross in Figure 2a_I, with a maximum of 8.85 ± 1.59 kg NO_2 km^{-2} h^{-1}). These fine-scale features are weak or even invisible in the bottom-up inventories, because of their lower spatial resolutions and lack of accurate spatial proxies to allocate provincial-level traffic emissions to individual locations.

In the Hetao Plain of Nei Monggol (Figure 2a−d_II), our data reveal high emissions along the G6 and G7 Highways. These signals are vague in MEIC and PKU-NO$_x$. EDGAR shows the emissions from G6 but not G7, likely because this section of G7 was not in operation in 2015 yet. The resolution of CEDS is too low to capture such traffic emissions. To the north of the highway section shared by G6 and G7, our data show emissions (with an average of 1.61 ± 0.64 kg NO_2 km^{-2} h^{-1}) from the towns and valleys close to the Wujia River where

most people in Bayannur City live. Again, these emissions are missing or not clear in the bottom-up inventories.

In west Xinjiang (Figure 2a−d_III), which covers the Aksu region and Kuqa City, our data show significant emissions around both the major roads and the minor roads; see SI Section 2 for definitions of the two road types. This information is not visible in MEIC, CEDS, and PKU-NO$_x$. EDGAR shows spotted emissions along the G3012 Highway crossing Aksu and Kuqa, and does not include emissions from the minor roads as well as nearby towns and villages. Our data also show large emissions in Baicheng County (with an average of 2.78 ± 0.79 kg NO_2 km^{-2} h^{-1}), which is an important place for extraction of rare-earth metal minerals. The emissions resulting from industrial, transportation and residential activities around Baicheng are absent in the bottom-up inventories.

We further examine the provincial emissions. The scatter plots in Figure 3 show that in Shanghai, Hubei, Zhejiang, and
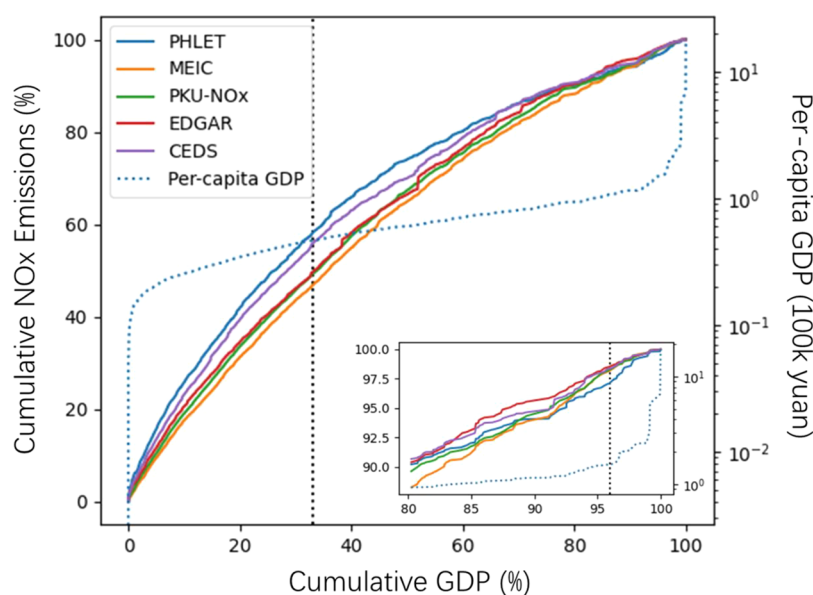
Figure 4. Cumulative NO_x emissions as a function of cumulative GDP across the counties. The counties are arranged from the lowest to the highest per-capita GDP. The blue dotted line standing for per-capita GDP refers to the *y*-axis on the right. The black dotted vertical line in the main figure indicates the counties with per-capita GDP below 50 thousand Yuan. The black dotted vertical line in the inlet indicates the counties with per-capita GDP higher than 150 thousand Yuan.

Guangdong, our emissions are significantly lower than the inventories. Provincial total of our emissions is lower than the average of the four inventories by 56.5% for Shanghai, 51.9% for Hubei, 43.6% for Guangdong, and 39.9% for Zhejiang. These differences are attributed to the uncertainties in our inversion and the inventories. On the one hand, our NO_x emissions might be underestimated in those provinces due to a possible overestimate in the NO_x lifetime. A test with the lifetime shortened by 30% (according to its uncertainty in SI Figure S5d) would increase the derived emissions by 30%. On the other hand, there are substantial differences among these inventories reflecting their individual uncertainties. Besides, these provinces may have experienced larger emission reductions than other provinces over the past few years, and this difference may not be captured in the inventories. According to the POMINO-OMI data,[29,30,47] from 2014 to 2019, the summertime mean NO_2 VCD decreases by 66.8% over Shanghai, 21.7% over Hubei, 27.2% over Zhejiang, and 36.1% over Guangdong, while the average NO_2 VCD over mainland China decreases by 14.0% only. By comparison, MEIC (from 2014 to 2017) and CEDS (from 2014 to 2019) do not show such stronger-than-national-average decreases over these provinces, and EDGAR and PKU-NO_x do not have data in recent years.

In the western provinces especially Xinjiang, Xizang, and Nei Monggol, our emissions are significantly higher than the bottom-up inventories. Quantitatively, our emissions are greater than the average of the four inventories by 195.2% in Xinjiang, 321.3% in Xizang, and 48.9% in Nei Monggol. This result is consistent with the comparison for fine-scale features (Figure 2) suggesting a large number of small-to-medium sources missed by the bottom-up inventories. A further analysis of spatial correlation with proxy data shows that our emission data have much stronger correlation with the density of minor roads over these western provinces than the inventories have (0.46 versus 0.23–0.37; SI Table S2). A respective analysis based on Tencent location data leads to a

similar finding (0.50 versus 0.28–0.45).(Note that PHLET emissions with and without proxy-based filtering show similar correlations with these proxies.) This suggests that the inventories miss emissions in small areas of human activity associated with the minor roads; for example, from on-road and off-road transportation, villages, and towns.

To confirm this point, we conduct two tests with our emission data. The first test removes our emissions at grid cells with minor roads but no major roads. It thus reduces the emissions by 74.5% over these three provinces and 21.3% over mainland China, and leads to much improved spatial correlation with the inventories (Figure 3 and SI Figure S11). The second test regrids our emissions to $0.25° \times 0.25°$ before removing the emissions. This leads to results (SI Figure S12) similar to the first test (SI Figure S11).

To further evaluate our emission data, we conduct two additional GEOS-Chem (v12.9.3, $0.25° \times 0.3125°$)[36] simulations in July 2019, using our emissions and MEIC, respectively. The results are compared with the Ministry of Ecology and Environment (MEE) surface NO_2 measurements at 1468 sites. The simulated monthly mean daily mean surface NO_2 concentrations based on our NO_x emissions show higher spatial correlation and a smaller bias ($R = 0.49$ and NMB = −45% versus $R = 0.46$ and NMB = −50%) (SI Figure S13). In the western, less affluent provinces such as Xinjiang, Xizang, and Nei Monggol, the simulation driven by our emissions achieves an even higher performance gain upon the simulation based on MEIC ($R = 0.54$ and NMB = −42% versus $R = 0.29$ and NMB = −74%). We note that the MEE NO_2 measurements are almost entirely for the urban areas and cannot be fully captured by GEOS-Chem simulations at $0.25° \times 0.3125°$. Also, the MEE NO_2 concentrations may be overestimated due to contamination from oxidized nitrogen species such as nitric acid and peroxyacyl nitrates.[48] Nevertheless, these comparisons support the advantage of our emission data especially in the less affluent areas.

Figure 4 shows how NO_x emissions cumulate with county-level GDP, after mapping the gridded data to each county and arranging the counties from the lowest to the highest affluence level (in terms of per-capita GDP). Compared to the inventories, our emission data show higher contributions (to the total in mainland China) from low-affluence counties. Specifically, counties with per-capita GDP lower than 50 thousand Yuan contribute 33% of the total GDP, but they contribute 58% of the total emission in our data, compared to 47% in MEIC, 50% in PKU-NO_x and EDGAR, and 56% in CEDS. This is because NO_x emissions from transportation and small-to-medium sources in these low-affluence counties are not well represented and often missing in the inventories, due to lack of detailed information (e.g., emission activities, emission factors, and locations) on these sources.[4]

The inlet of Figure 4 highlights the contributions of most affluent counties to the total emission of mainland China. Counties with per-capita GDP larger than 150 thousand Yuan contribute 4% of the total GDP and 3% of the total emission according to our data set, in contrast to 2% for MEIC, PKU-NO_x and EDGAR, and 1% for CEDS. This is likely because transportation emissions are not well captured in the inventories.

■ DISCUSSION

This study improves our PHLET-based inversion approach to estimate NO_x emissions at a high horizontal resolution (5 km) for East Asia based on TROPOMI-POMINO NO_2 VCD data. Our inversion approach accounts for the effects of horizontal transport and nonlinear NO_x chemistry for each location. A focused emission analysis is done for mainland China, facilitated by five spatial proxy data sets of human activity. Our emission data reveal fine spatial structures, transportation signals and many small-to-medium sources which are missing or poorly represented in four widely used bottom-up emission inventories.

To date, China's effort to reduce emissions has focused on more developed regions especially in the east,[49] in part guided by bottom-up emission inventories. However, our emissions reveal numerous small-to-medium sources in less affluent counties with relatively low per-capita GDP, and these sources are often missing in the inventories. In the future, emissions in less affluent areas might experience further increases if the industries move to these areas,[50] for example, as a result of industrial restructuring and/or as a response of enterprises to strengthening emission control in more affluent regions.[51,52] Therefore, effective, targeted control measures to reduce small-to-medium emission sources in less-affluent areas are an important further step to protect China's atmospheric environment. To this end, our high-resolution emission data offer a reference to help track and reduce emissions at places where bottom-up emission inventories are less reliable.

Our retrieval algorithm can be further improved. First, our retrieval constrains daily mean emissions using satellite NO_2 VCDs in the early afternoon.[17,19,20,37−39] This is a common practice for polar orbiting satellite-based emission constraint at any horizontal resolutions. Previous studies have shown that when proper retrieval approaches are used, emissions inferred from morning satellite measurements are within 10% of those inferred from measurements in the afternoon.[53] This offers some confidence that the intrinsic problem of polar orbiting satellite remote sensing (i.e., it lacks diurnal variability information) has a limited effect on the emission constraint.

Geostationary satellite remote sensing such as the Geostationary Environment Monitoring Spectrometer (GEMS)[54,55] is expected to provide much more information on the diurnal variation of NO_2, useful for emission constraint. Note that the diurnal variability of emissions is also not or poorly represented in bottom-up emission inventories, including those analyzed in this study. Second, although our emissions show many high-resolution details of the NO_x emission distribution, they alone cannot tell the exact source types. This is another common limitation of top-down emissions. Combining top-down emissions with sectorally detailed bottom-up data and/or local surveys will be useful to identify source types for targeted emission control.

Our emission inversion approach is a fast algorithm. After all input data are prepared, the emission inversion for the whole study domain takes about 900 core-hours. And since the calculation is highly parallelized by dividing the study domain into subdomains, it only takes several actual hours to derive the NO_x emissions for the whole domain. The reliability and low cost mean that the approach can be applied to the globe and other years, allowing a low-cost, timely and reliable derivation of NO_x emissions, variabilities and trends at a fine spatial scale.

■ ASSOCIATED CONTENT

Ⓢ Supporting Information

The Supporting Information is available free of charge at https://pubs.acs.org/doi/10.1021/acs.est.1c07723.

> Examples for interpolated NO_2 profiles (Figure S1); NO_2 VCDs before/after adjustments (Figure S2); Regression model evaluation and predicted NO_2/NO_x ratio (Figure S3); Illustration of subdomains (Figure S4); NO_x lifetime and uncertainties of NO_x lifetime and emissions (Figure S5); Evaluation of emission inversion approach based on GEOS-Chem simulations (Figure S6); Evaluation of emission inversion approach based on GEOS-Chem simulations with the AKs applied (Figure S7); Natural NO_x emissions (Figure S8); Proxy data of human activity (Figure S9); Our NO_x emissions at lower resolutions (Figure S10); Scatter plots of provincial NO_x emissions after removing minor roads from our emissions (Figure S11); Scatter plots of provincial NO_x emissions after regridding our emissions to 0.25° × 0.25° and removing minor roads from our emissions (Figure S12); GEOS-Chem simulations based on our emissions and MEIC and comparison with MEE measurements (Figure S13);Provincial NO_x emission amounts (Figure S14); Fitted coefficients for regression for NO_2/NO_x ratio (Table S1); Uncertainty description (Table S2); Correlation between proxies and emissions (Table S3); Model description of GEOS-Chem (Section 1); Description of proxy data of human activity (Section 2) (PDF)

■ AUTHOR INFORMATION

Corresponding Author

Jintai Lin − *Laboratory for Climate and Ocean-Atmosphere Studies, Department of Atmospheric and Oceanic Sciences, School of Physics, Peking University, Beijing 100871, China;* ⓞ orcid.org/0000-0002-2362-2940; Phone: +86-010-62767973; Email: linjt@pku.edu.cn

Authors

Hao Kong − *Laboratory for Climate and Ocean-Atmosphere Studies, Department of Atmospheric and Oceanic Sciences, School of Physics, Peking University, Beijing 100871, China;* orcid.org/0000-0001-5038-2914

Lulu Chen − *Laboratory for Climate and Ocean-Atmosphere Studies, Department of Atmospheric and Oceanic Sciences, School of Physics, Peking University, Beijing 100871, China;* orcid.org/0000-0002-8929-3414

Yuhang Zhang − *Laboratory for Climate and Ocean-Atmosphere Studies, Department of Atmospheric and Oceanic Sciences, School of Physics, Peking University, Beijing 100871, China*

Yingying Yan − *Department of Atmospheric Science, School of Environmental Sciences, China University of Geosciences (Wuhan), Wuhan 430074, China*

Mengyao Liu − *R&D Satellite Observations Department, Royal Netherlands Meteorological Institute, De Bilt NL-3731 GA, The Netherlands*

Ruijing Ni − *Laboratory for Climate and Ocean-Atmosphere Studies, Department of Atmospheric and Oceanic Sciences, School of Physics, Peking University, Beijing 100871, China;* orcid.org/0000-0003-3072-6817

Zehui Liu − *Laboratory for Climate and Ocean-Atmosphere Studies, Department of Atmospheric and Oceanic Sciences, School of Physics, Peking University, Beijing 100871, China*

Hongjian Weng − *Laboratory for Climate and Ocean-Atmosphere Studies, Department of Atmospheric and Oceanic Sciences, School of Physics, Peking University, Beijing 100871, China*

Complete contact information is available at:
https://pubs.acs.org/10.1021/acs.est.1c07723

Author Contributions

J.L. conceived the research. J.L. and H.K. designed the research. H.K. performed the data processing, model development, and simulations. Y.Z. and M.L. contributed to processing of POMINO-TROPOMI NO$_2$ VCDs. L.C., Y.Y., R.N., and H.W. contributed to the setting of GEOS-Chem. Z.L. contributed to the model setting when revising the paper. H.W. provided soil NO$_x$ emissions. L.C., Y.Y., and R.N. contributed to the writing. H.K. and J.L. analyzed the results and wrote the paper.

Notes

The authors declare no competing financial interest.

■ REFERENCES

(1) Seinfeld, J. H.; Pandis, S. N. *Atmospheric Chemistry and Physics: From Air Pollution to Climate Change*; Wiley, 1998; pp 37−38.

(2) Lin, J. T. Satellite constraint for emissions of nitrogen oxides from anthropogenic, lightning and soil sources over East China on a high-resolution grid. *Atmospheric Chemistry and Physics* **2012**, *12* (6), 2881−2898.

(3) Zhao, Y.; Nielsen, C. P.; Lei, Y.; McElroy, M. B.; Hao, J. Quantifying the uncertainties of a bottom-up emission inventory of anthropogenic atmospheric pollutants in China. *Atmospheric Chemistry and Physics* **2011**, *11* (5), 2295−2308.

(4) Zheng, B.; Cheng, J.; Geng, G.; Wang, X.; Li, M.; Shi, Q.; Qi, J.; Lei, Y.; Zhang, Q.; He, H. Mapping anthropogenic emissions in China at 1 km spatial resolution and its application in air quality modeling. *Science Bulletin* **2021**, *66* (6), 612−620.

(5) Geng, G.; Zhang, Q.; Martin, R. V.; Lin, J.; Huo, H.; Zheng, B.; Wang, S.; He, K. Impact of spatial proxies on the representation of bottom-up emission inventories: A satellite-based analysis. *Atmospheric Chemistry and Physics* **2017**, *17* (6), 4131−4145.

(6) Zheng, B.; Zhang, Q.; Tong, D.; Chen, C.; Hong, C.; Li, M.; Geng, G.; Lei, Y.; Huo, H.; He, K. Resolution dependence of uncertainties in gridded emission inventories: a case study in Hebei, China. *Atmospheric Chemistry and Physics* **2017**, *17* (2), 921−933.

(7) Center for International Earth Science Information Network - CIESIN - Columbia University. *Gridded Population of the World, Version 4 (GPWv4): Population Count*; NASA Socioeconomic Data and Applications Center (SEDAC): Palisades, NY, 2016.

(8) Leue, C.; Wenig, M.; Wagner, T.; Klimm, O.; Platt, U.; Jähne, B. Quantitative analysis of NO$_x$ emissions from Global Ozone Monitoring Experiment satellite image sequences. *Journal of Geophysical Research: Atmospheres* **2001**, *106* (D6), 5493−5505.

(9) Lin, J. T.; Liu, Z.; Zhang, Q.; Liu, H.; Mao, J.; Zhuang, G. Modeling uncertainties for tropospheric nitrogen dioxide columns affecting satellite-based inverse modeling of nitrogen oxides emissions. *Atmospheric Chemistry and Physics* **2012**, *12* (24), 12255−12275.

(10) Lin, J. T.; McElroy, M. B. Detection from space of a reduction in anthropogenic emissions of nitrogen oxides during the Chinese economic downturn. *Atmospheric Chemistry and Physics* **2011**, *11* (15), 8171−8188.

(11) Lin, J. T.; McElroy, M. B.; Boersma, K. F. Constraint of anthropogenic NO$_x$ emissions in China from different sectors: a new methodology using multiple satellite retrievals. *Atmospheric Chemistry and Physics* **2010**, *10*, 63−78.

(12) Martin, R. V., Global inventory of nitrogen oxide emissions constrained by space-based observations of NO$_2$ columns. *J. Geophys. Res.* **2003**, *108* (D17). DOI: 10.1029/2003JD003453

(13) Zhao, C.; Wang, Y. Assimilated inversion of NO$_x$ emissions over east Asia using OMI NO$_2$ column measurements. *Geophys. Res. Lett.* **2009**, *36* (6), L06805.

(14) Mijling, B.; van der A, R. J.; Zhang, Q. Regional nitrogen oxides emission trends in East Asia observed from space. *Atmospheric Chemistry and Physics* **2013**, *13* (23), 12003−12012.

(15) Miyazaki, K.; Eskes, H.; Sudo, K.; Boersma, K. F.; Bowman, K.; Kanaya, Y. Decadal changes in global surface NO$_x$ emissions from multi-constituent satellite data assimilation. *Atmospheric Chemistry and Physics Discussions* **2017**, *17*, 1−48.

(16) Qu, Z.; Henze, D. K.; Capps, S. L.; Wang, Y.; Xu, X.; Wang, J.; Keller, M. Monthly top-down NOx emissions for China (2005−2012): A hybrid inversion method and trend analysis. *Journal of Geophysical Research Atmospheres* **2017**, *122*, 4600−4625.

(17) Beirle, S.; Boersma, K. F.; Platt, U.; Lawrence, M. G.; Wagner, T. Megacity Emissions and Lifetimes of Nitrogen Oxides Probed from Space. *Science* **2011**, *333* (6050), 1737−1739.

(18) Beirle, S.; Borger, C.; Dörner, S.; Eskes, H.; Kumar, V.; de Laat, A.; Wagner, T. Catalog of NOx emissions from point sources as derived from the divergence of the NO2 flux for TROPOMI. *Earth Syst. Sci. Data* **2021**, *13* (6), 2995−3012.

(19) Beirle, S.; Borger, C.; Dörner, S.; Li, A.; Hu, Z.; Liu, F.; Wang, Y.; Wagner, T. Pinpointing nitrogen oxide emissions from space. *Science Advances* **2019**, *5*, eaax9800.

(20) Kong, H.; Lin, J.; Zhang, R.; Liu, M.; Weng, H.; Ni, R.; Chen, L.; Jingxu, W.; Yan, Y.; Zhang, Q. High-resolution (0.05° × 0.05°) NO x emissions in the Yangtze River Delta inferred from OMI. *Atmospheric Chemistry and Physics* **2019**, *19*, 12835−12856.

(21) Sun, K.; Li, L.; Jagini, S.; Li, D. A satellite-data-driven framework to rapidly quantify air-basin-scale NOx emissions and its application to the Po Valley during the COVID-19 pandemic. *Atmos. Chem. Phys.* **2021**, *21* (17), 13311−13332.

(22) Geffen, J. H. G. M. v.; Eskes, H. J.; Boersma, K. F.; Veefkind, J. P.; Maasakkers, J. D. *TROPOMI ATBD of the Total and Tropospheric NO₂ Data Products*; Royal Netherlands Meteorological Institute, Ministry of Infrastructure and Water Management, 2019.

(23) Veefkind, P.; Aben, I.; McMullan, K.; Förster, H.; Vries, J.; Otter, G.; Claas, J.; Eskes, H.; Dehaan, J.; Kleipool, Q.; van Weele, M.; Hasekamp, O.; Hoogeveen, R. W. M.; Landgraf, J.; Snel, R.; Tol, P.; Ingmann, P.; Voors, R.; Kruizinga, B.; Levelt, P. TROPOMI on the ESA Sentinel-5 Precursor: A GMES mission for global observations of the atmospheric composition for climate, air quality and ozone layer applications. *Remote Sensing of Environment* 2012, 120, 70−83.

(24) Liu, M.; Lin, J.; Kong, H.; Boersma, K. F.; Eskes, H.; Kanaya, Y.; He, Q.; Tian, X.; Qin, K.; Xie, P.; Spurr, R.; Ni, R.; Yan, Y.; Weng, H.; Wang, J. A new TROPOMI product for tropospheric NO₂ columns over East Asia with explicit aerosol corrections. *Atmos. Meas. Technol.* 2020, 13 (8), 4247−4259.

(25) Eskes, H. J.; Eichmann, K. U.; Lambert, J. C.; Loyola, D.; Veefkind, J. P.; Dehn, A.; Zehner, C. *S5P Mission Performance Centre Nitrogen Dioxide [L2__NO₂____] Readme*, version 01.03.00; Royal NetherlandsMeteorological Institute (KNMI): De Bilt, the Netherlands, 2019.

(26) Griffin, D.; Zhao, X.; McLinden, C. A.; Boersma, F.; Bourassa, A.; Dammers, E.; Degenstein, D.; Eskes, H.; Fehr, L.; Fioletov, V.; Hayden, K.; Kharol, S. K.; Li, S.-M.; Makar, P.; Martin, R. V.; Mihele, C.; Mittermeier, R. L.; Krotkov, N.; Sneep, M.; Lamsal, L. N.; Linden, M. t.; Geffen, J. v.; Veefkind, P.; Wolde, M. High-Resolution Mapping of Nitrogen Dioxide With TROPOMI: First Results and Validation Over the Canadian Oil Sands. *Geophys. Res. Lett.* 2019, 46 (2), 1049−1060.

(27) Lin, J.-T.; Liu, M.-Y.; Xin, J. Y.; Boersma, K. F.; Spurr, R.; Martin, R.; Zhang, Q. Influence of aerosols and surface reflectance on satellite NO₂ retrieval: seasonal and spatial characteristics and implications for NOₓ emission constraints. *Atmospheric Chemistry and Physics* 2015, 15 (19), 11217−11241.

(28) Lin, J. T.; Martin, R. V.; Boersma, K. F.; Sneep, M.; Stammes, P.; Spurr, R.; Wang, P.; Van Roozendael, M.; Clémer, K.; Irie, H. Retrieving tropospheric nitrogen dioxide from the Ozone Monitoring Instrument: Effects of aerosols, surface reflectance anisotropy, and vertical profile of nitrogen dioxide. *Atmospheric Chemistry and Physics* 2014, 14 (3), 1441−1461.

(29) Liu, M.; Lin, J.; Boersma, K. F.; Pinardi, G.; Wang, Y.; Chimot, J.; Wagner, T.; Xie, P.; Eskes, H.; Van Roozendael, M.; Hendrick, F.; Wang, P.; Wang, T.; Yan, Y.; Chen, L.; Ni, R. Improved aerosol correction for OMI tropospheric NO₂ retrieval over East Asia: constraint from CALIOP aerosol vertical profile. *Atmospheric Measurement Techniques* 2019, 12 (1), 1−21.

(30) Lin, J. T.; Liu, M. Y.; Xin, J. Y.; Boersma, K. F.; Spurr, R.; Martin, R.; Zhang, Q. Influence of aerosols and surface reflectance on satellite NO₂ retrieval: seasonal and spatial characteristics and implications for NOₓ emission constraints. *Atmospheric Chemistry and Physics* 2015, 15 (19), 11217−11241.

(31) van Geffen, J.; Eskes, H.; Compernolle, S.; Pinardi, G.; Verhoelst, T.; Lambert, J. C.; Sneep, M.; ter Linden, M.; Ludewig, A.; Boersma, K. F.; Veefkind, J. P. Sentinel-5P TROPOMI NO₂ retrieval: impact of version v2.2 improvements and comparisons with OMI and ground-based data. *Atmos. Meas. Technol. Discuss.* 2021, 2021, 1−37.

(32) Beirle, S.; Boersma, K.; Platt, U.; Lawrence, M.; Wagner, T. Megacity Emissions and Lifetimes of Nitrogen Oxides Probed from Space. *Science (New York, N.Y.)* 2011, 333, 1737−9.

(33) Lucchesi, R., File Specification for GEOS FP. GMAO Office Note No. 4 (Version 1.2).2018. http://gmao.gsfc.nasa.gov/pubs/office_notes.

(34) Yuan, H.; Dai, Y.; Xiao, Z.; Ji, D.; Shangguan, W. Reprocessing the MODIS Leaf Area Index products for land surface and climate modelling. *Remote Sensing of Environment* 2011, 115 (5), 1171−1187.

(35) Yuan, H.; Dai, Y.; Xiao, Z. *Reprocessed MODIS Version 6 Leaf Area Index data sets for land surface and climate modelling*; Sun Yat-sen University, 2020.

(36) The International GEOS-Chem User Community. geoschem/geos-chem: GEOS-Chem 12.9.3 (12.9.3).; Zenodo: 2020.

(37) Beirle, S.; Sihler, H.; Wagner, T. Mapping NOₓ Sources on High Spatial Resolution by Combined Measurements from OMI and GOME-2 Narrow Swath Mode, ATMOS 2015. In *Proceedings of the Conference held 8−12 June, Crete*; Ouwehand, L., Ed., 2015.

(38) Liu, F.; Beirle, S.; Zhang, Q.; Dörner, S.; He, K.; Wagner, T. NOₓ lifetimes and emissions of cities and power plants in polluted background estimated by satellite observations. *Atmospheric Chemistry and Physics* 2016, 16 (8), 5283−5298.

(39) Liu, F.; Beirle, S.; Zhang, Q.; van der A, R. J.; Zheng, B.; Tong, D.; He, K. NOx emission trends over Chinese cities estimated from OMI observations during 2005 to 2015. *Atmospheric Chemistry and Physics* 2017, 17 (15), 9261−9275.

(40) Weng, H.; Lin, J.; Martin, R.; Millet, D. B.; Jaeglé, L.; Ridley, D.; Keller, C.; Li, C.; Du, M.; Meng, J. Global high-resolution emissions of soil NOx, sea salt aerosols, and biogenic volatile organic compounds. *Scientific Data* 2020, 7 (1), 148.

(41) Giglio, L.; Randerson, J. T.; van der Werf, G. R. Analysis of daily, monthly, and annual burned area using the Fourth-Generation Global Fire Emissions Database (GFED4). *Journal of Geophysical Research: Biogeosciences* 2013, 118 (1), 317−328.

(42) Liu, F.; Zhang, Q.; Tong, D.; Zheng, B.; Li, M.; Huo, H.; He, K. B. High-resolution inventory of technologies, activities, and emissions of coal-fired power plants in China from 1990 to 2010. *Atmospheric Chemistry and Physics* 2015, 15 (23), 13299−13317.

(43) Zheng, B.; Huo, H.; Zhang, Q.; Yao, Z. L.; Wang, X. T.; Yang, X. F.; Liu, H.; He, K. B. High-resolution mapping of vehicle emissions in China in 2008. *Atmospheric Chemistry and Physics* 2014, 14, 9787−9805.

(44) Crippa, M.; Solazzo, E.; Huang, G.; Guizzardi, D.; Koffi, E.; Muntean, M.; Schieberle, C.; Friedrich, R.; Janssens-Maenhout, G. High resolution temporal profiles in the Emissions Database for Global Atmospheric Research. *Scientific Data* 2020, 7, 121.

(45) Feng, L.; Smith, S. J.; Braun, C.; Crippa, M.; Gidden, M. J.; Hoesly, R.; Klimont, Z.; van Marle, M.; van den Berg, M.; van der Werf, G. R. The generation of gridded emissions data for CMIP6. *Geosci. Model Dev.* 2020, 13 (2), 461−482.

(46) Huang, T.; Zhu, X.; Zhong, Q.; Yun, X.; Meng, W.; Li, B.; Ma, J.; Zeng, E. Y.; Tao, S. Spatial and Temporal Trends in Global Emissions of Nitrogen Oxides from 1960 to 2014. *Environ. Sci. Technol.* 2017, 51 (14), 7992−8000.

(47) Liu, M.-Y.; Lin, J.-T.; Wang, Y.-C.; Sun, Y.; Zheng, B.; Shao, J.; Chen, L.-L.; Zheng, Y.; Chen, J.; Fu, T. M.; Yan, Y.-Y.; Zhang, Q.; Wu, Z. Spatiotemporal variability of NO₂ and PM₂.₅ over Eastern China: observational and model analyses with a novel statistical method. *Atmospheric Chemistry and Physics* 2018, 18 (17), 12933−12952.

(48) Liu, M.; Lin, J.; Wang, Y.; Sun, Y.; Zheng, B.; Shao, J.; Chen, L.; Zheng, Y.; Chen, J.; Fu, T.-M.; Yan, Y.; Zhang, Q.; Wu, Z. Spatiotemporal variability of NO₂ and PM₂.₅ over Eastern China: observational and model analyses with a novel statistical method. *Atmospheric Chemistry and Physics Discussions* 2018, 18, 1−34.

(49) Jiang, L.; Chen, Y.; Zhou, H.; He, S. NOx emissions in China: Temporal variations, spatial patterns and reduction potentials. *Atmospheric Pollution Research* 2020, 11 (9), 1473−1480.

(50) Cui, Y.; Lin, J.; Song, C.; Liu, M.; Yan, Y.; Xu, Y.; Huang, B. Rapid growth in nitrogen dioxide pollution over Western China, 2005−2013. *Atmos. Chem. Phys.* 2016, 16 (10), 6207−6221.

(51) Zhao, H.; Li, X.; Zhang, Q.; Jiang, X.; Lin, J.; Peters, G.; Li, M.; Geng, G.; Zheng, B.; Huo, H.; Zhang, L.; Davis, S.; He, K. Effects of atmospheric transport and trade on air pollution mortality in China. *Atmospheric Chemistry and Physics Discussions* 2017, 17, 1−23.

(52) Fang, D.; Chen, B.; Hubacek, K.; Ni, R.; Chen, L.; Feng, K.; Lin, J., Clean air for some: Unintended spillover effects of regional air pollution policies. *Science Advances* 2019 5 (4), eaav4707.

(53) Gu, D.; Wang, Y.; Smeltzer, C.; Boersma, K. F. Anthropogenic emissions of NOₓ over China: Reconciling the difference of inverse

modeling results using GOME-2 and OMI measurements. *Journal of Geophysical Research: Atmospheres* **2014**, *119* (12), 7732−7740.

(54) Kim, J.; Jeong, U.; Ahn, M.-H.; Kim, J.; Park, R.; Lee, H.; Song, C.; Choi, Y.-S.; Lee, K.; Yoo, J.-M.; Jeong, M.-J.; Park, S. K.; Lee, K.-M.; Song, C.-K.; Kim, S.-W.; Kim, Y.; Kim, S.-W.; Kim, M.; Go, S.; Choi, Y. New Era of Air Quality Monitoring from Space: Geostationary Environment Monitoring Spectrometer (GEMS). *Bulletin of the American Meteorological Society* **2020**, *101*, 00.

(55) Lasnik, J.; Stephens, M.; Baker, B.; Randall, C.; Ko, D. H.; Kim, S.; Kim, Y.; Lee, E. S.; Chang, S.; Park, J. M. In *Geostationary Environment Monitoring Spectrometer (gems) Over the Korea Peninsula and Asia-Pacific Region*, August Fall Meeting, 2014.